HOSTED BY

ELSEVIER

CrossMark

Available online at www.sciencedirect.com

ScienceDirect

Journal of Magnesium and Alloys 2 (2014) 245–256
www.elsevier.com/journals/journal-of-magnesium-and-alloys/2213-9567

Full length article

Corrosion behavior of Mg–Gd–Zn based alloys in aqueous NaCl solution

A. Srinivasan [a,b,*], C. Blawert [a], Y. Huang [a], C.L. Mendis [a], K.U. Kainer [a], N. Hort [a]

[a] *Helmholtz-Zentrum, Geesthacht, Institute of Materials Research, Max-Planck-Str. 1, 21502 Geesthacht, Germany*
[b] *CSIR-National Institute for Interdisciplinary Science and Technology, Pappanamcode (P.O), Thiruvananthapuram 695 019, India*

Received 3 June 2014; revised 23 June 2014; accepted 11 August 2014
Available online 16 October 2014

Abstract

The corrosion behavior of Mg-10Gd–xZn (x = 2, 6 wt.%) alloys in 0.5 wt.% NaCl solution was investigated. Microstructures of both the alloys consisted of $(Mg,Zn)_3Gd$ phase and lamellar long period stacking ordered (LPSO) phase. The morphology of the second phase at the grain boundary differed in both alloys: it was a continuous network structure in Mg–10Gd–6Zn, whereas it was relatively discrete in Mg–10Gd–2Zn. The dendrites were finer in size and highly branched in Mg–10Gd–6Zn. The corrosion results indicated that the increase in Zn content increased the corrosion rate in Mg–10Gd–xZn alloys. Micro-galvanic corrosion occurred near the grain boundary in both alloys initially as the grain boundary phase was stable and acted as a cathode, however, filiform corrosion dominated in the later stage, which was facilitated by the LPSO phase in the matrix. Severe micro-galvanic corrosion occurred in Mg–10Gd–6Zn due to the higher volume of second phase. The stability of the second phase at the grain boundary was altered and dissolved after the long immersion times. Probably the NaCl solution chemically reacted with the grain boundary phase and de-stabilized it during the long immersion times, and was removed by the chromic acid used for the corrosion product removal.

Keywords: Mg–Gd–Zn alloys; Micro-galvanic corrosion; Polarization; Electrochemical characterization

1. Introduction

Magnesium alloys have many attractive properties such as low density, high specific strength, good castability, excellent machinability and weldability. However, its low resistance to creep and corrosion are two important drawbacks. Magnesium alloys have poor corrosion resistance compared to aluminum alloys as magnesium is a reactive metal. Designing magnesium alloys with high corrosion and creep resistance, therefore, is a challenging task. The most widely used Mg–Al based alloys such as AZ91, AM50, exhibit high corrosion resistance, but, the poor creep resistance limits their applications at elevated temperature. Many alloys developed for high temperature applications such as power train components in automobiles failed to make an impact as most of these alloys display poor corrosion resistance.

Rare earth (RE) containing Mg alloys exhibiting superior high temperature properties are considered as potential candidates for automobile applications [1]. However, the corrosion behavior of Mg-RE alloys is not well understood. It is well documented that the RE additions improve the corrosion resistance of Mg–Al based alloys [2,3]. Addition of RE reduces the β-$Mg_{17}Al_{12}$ phase in these alloys thereby reducing the micro-galvanic sites that results in improved corrosion resistance. Additionally, RE can react with impurities such as Fe and Cu resulting in a ‘cleaning effect’ of the melt [4].

* Corresponding author. CSIR-National Institute for Interdisciplinary Science and Technology, Pappanamcode (P.O), Thiruvananthapuram 695 019, India. Tel.: +91 471 2515248; fax: +91 471 2491712.
E-mail addresses: srininiist@gmail.com (A. Srinivasan), carsten.blawert@hzg.de (C. Blawert), yuanding.huang@hzg.de (Y. Huang), chamini.mendis@hzg.de (C.L. Mendis), karl.kainer@hzg.de (K.U. Kainer), norbert.hort@hzg.de (N. Hort).
Peer review under responsibility of National Engineering Research Center for Magnesium Alloys of China, Chongqing University.

http://dx.doi.org/10.1016/j.jma.2014.08.002.

Formation of stable film on the corroding surface is also observed with the RE additions [5]. Collectively these factors improve the corrosion resistance of Mg–Al alloys. However, Mg-RE based intermetallic phases that appear on the as cast microstructure of Mg-RE based alloys (RE as a major elements) act as cathodic sites for the micro-galvanic corrosion, and results in poor corrosion resistance [6,7]. In contrast, solution treatment that results in the complete dissolution of the second phases and uniform distribution of RE elements in the magnesium matrix, greatly improves the corrosion resistance. It was also reported that the combination of RE and Zn in magnesium alloys lead to poor corrosion resistance [8].

There are two groups of RE elements considered for magnesium alloys: (i) low solubility (Nd, Ce, La) (ii) high solubility (Y, Gd, Dy) elements. In recent years, magnesium alloys with high soluble RE elements became more popular due to their superior creep properties. Many alloys such as Mg–Y, Mg–Gd, Mg–Dy are developed and their mechanical properties are studied [9,10]. Gd, which has high solubility in magnesium (23.5 wt.% at eutectic temperature), is shown to be a potential RE element for improving mechanical properties of magnesium alloys, even at higher temperatures [9]. Many experimental alloy systems such as Mg–Gd–Y, Mg–Gd–Y–Nd, Mg–Gd–Zn, Mg–Gd–Y–Zn are developed and their microstructure and mechanical properties are investigated [11–13]. Among these systems, Mg–Gd–Zn is one of the very important systems as its microstructure consists of a number of different phases, such as I, W, Z and laves phases, depending upon the ratio of Zn and Gd content, and hence resulting in different mechanical behavior [14]. Moreover, long period stacking ordered (LPSO) structures are also identified in this system, which enhances the mechanical properties and the heat resistance. There are many investigations on the mechanical behavior of Mg–Gd–Zn alloys, but not many detailed studies on their corrosion behavior have been reported. Hence, in the present investigation, the microstructural dependence of corrosion in two Mg–Gd–Zn alloys i.e, Mg–10Gd–2Zn and Mg–10Gd–6Zn (all are in weight percentages) were investigated.

2. Materials and methods

2.1. Casting

The alloys of the present investigation were prepared in a resistance tilt furnace under a protective gas mixture of Ar + 2% SF_6. Pure Mg, Zn and Gd ingots were used to prepare the alloys. Initially the required amounts of Mg and Zn were melted in a mild steel crucible, and Gd was added into the melt at 770 °C. After the addition, the melt was stirred mechanically at 200 rpm for 30 min. for the complete dissolution of Gd and to make a uniform composition throughout the melt. The melt was poured into a pre-heated (350 °C) metallic round mold with an inner diameter of 100 mm and a length of 400 mm attached with a sprue at the top. The analyzed chemical compositions of the major alloying elements and important impurities of the castings and the alloy code for the easy reference are presented in Table 1. The Gd contents were analyzed in X-ray fluorescence analyzer (XRF). Zn contents were measured in optical emission spectroscope (OES) whereas other impurities contents were analyzed using integrated coupled plasma optical emission spectroscopy (ICP-OES).

2.2. Microstructure

Samples for the microstructure studies were prepared by grinding on different grades of emery papers from 80 to 2400 grits followed by final polishing with 0.05 μm colloidal silica (OPS). The samples were chemically etched in picral solution (8 g picric acid, 5 ml acetic acid, 10 ml distilled water and 100 ml ethanol), and examined under light microscope (Reichert-Jung MeF3) attached with a digital camera controlled by analySIS pro software. Polished samples were also examined in a Zeiss Ultra 55 (Carl Zeiss GmbH, Oberkochen, Germany) scanning electron microscope (SEM) attached with Electron Dispersive X-ray Spectroscope (EDX). The specimens for TEM were mechanically ground to about 400 μm in thickness, and 3 mm diameter discs were then cut using an abrasive slurry disc cutter. These discs were mechanically ground to 120 μm in thickness, and further thinned by twin-jet electro polishing in a solution of 1.5% $HClO_4$ and 98.5% ethanol at −45 °C and 40 V. The TEM examinations were carried out on a Philips CM 200 operating at 200 kV.

2.3. Corrosion studies

2.3.1. H_2 measurement (eudiometer study)

All the corrosion tests were conducted at room temperature in 0.5 wt.% NaCl solution. Immersion tests were carried out in a standard eudiometer apparatus with a total volume of 400 ml and a resolution of 0.5 ml. Cubic samples of size $14 \times 14 \times 14$ mm^3 were used for eudiometer studies. All sides of the samples were ground on emery papers up to 1200 grit size and the surfaces were degreased with ethanol prior to the testing. The corrosion rate (C_R) at the end of the eudiometer test was calculated in mm per year by converting the total amount of collected hydrogen into material loss (1 ml of H_2 gas = 0.001083 g of dissolved Mg) and using the equation [15]:

$$C_R = \frac{8.76 \times 10^4 \times \Delta g}{A \times t \times \rho} \quad (1)$$

where, Δg is weight loss in g (in case of eudiometer study, Δg = 0.001083 * H_2 volume), A is surface area exposed

Table 1
Chemical composition of alloys.

Nominal composition (wt.%) and alloy code	Analyzed compositions (wt.%)				
	Gd	Zn	Fe	Ni	Cu
Mg–10Gd–2Zn (Alloy 1)	9.11	2.29	0.0022	0.0002	0.0042
Mg–10Gd–6Zn (Alloy 2)	8.65	6.61	0.0023	0.0002	0.0050

in cm^2, t is total immersion time in h and ρ is density of the alloy in g/cm^3.

Three tests were conducted for each alloy and the average values are reported. The corrosion rates were calculated also by measuring the weight loss at the end of the eudiometric test after removing the corrosion product by immersing the samples in a chromic acid (180 g/l) at room temperature for 30–40 min. using the Eq. (1). Additionally, samples were immersed for different times and their corrosion morphologies were studied SEM.

2.3.2. Polarization and electrochemical impedance spectroscopy (EIS) measurements

Electrochemical corrosion tests were conducted using a computer controlled Gill AC potentiostat/frequency response analyzer with the three-electrode cells of saturated Ag/AgCl (saturated with KCl) as a reference electrode, platinum mesh as a counter electrode and sample as the working electrode. The electrolyte was magnetically stirred at a constant temperature of 22 ± 1 °C during the measurement. Specimens were immersed for 0.5 h in the electrolyte to reach relative stable potentials and the free corrosion potential was monitored. The potentiodynamic polarization scan was measured from −200 mV relative to the free corrosion potential with a scan rate of 0.2 mV/s. The test was terminated when the corrosion current density reached to 0.1 mA/cm^2. The corrosion current density (i_{corr}) and corrosion potential ($E_{corr,}$ vs Ag/AgCl) were measured from the Tafel plot. Polarization measurements were conducted at different immersion times, 0.5 h, 24 h and 100 h. The impedance measurements on the samples were performed at their open circuit potential with AC amplitude of 10 mV in the frequency range from 10^4 to 10^{-2} Hz. The measurements were performed at different intervals, 0 h, 1 h, 6 h, 12 h and 24 h. The results in the form of Nyquist and Bode plots were analyzed using the free EIS Spectrum Analyzer software [16]. At least two tests were conducted for each condition to confirm the validity of the polarization and EIS measurements.

3. Results

3.1. As cast microstructure

Fig. 1 shows the SEM micrographs of alloy 1. The microstructure of alloy 1 exhibited columnar dendrites (Fig. 1(a)), and at a higher magnification, the microstructure (Fig. 1(b)) indicated two different types of phases located mostly at the interdendritic regions. The major phase marked as 'A' in Fig. 1(b) had rib bone like morphology. The other phase, marked as 'B', was relatively smaller in size, and was a solid block. EDX analysis of the phase 'A' indicated that the phase consistently contained slightly higher Gd than Zn content. The typical composition of the phase was 56.97 at.% Mg, 21.97 at.% Gd, 19.47 at.% Zn. The TEM analysis of the phase presented in Fig. 1(c) confirmed that the phase was face centre cubic (fcc) Mg_3Gd type with lattice parameter 'a' = 0.726 nm,

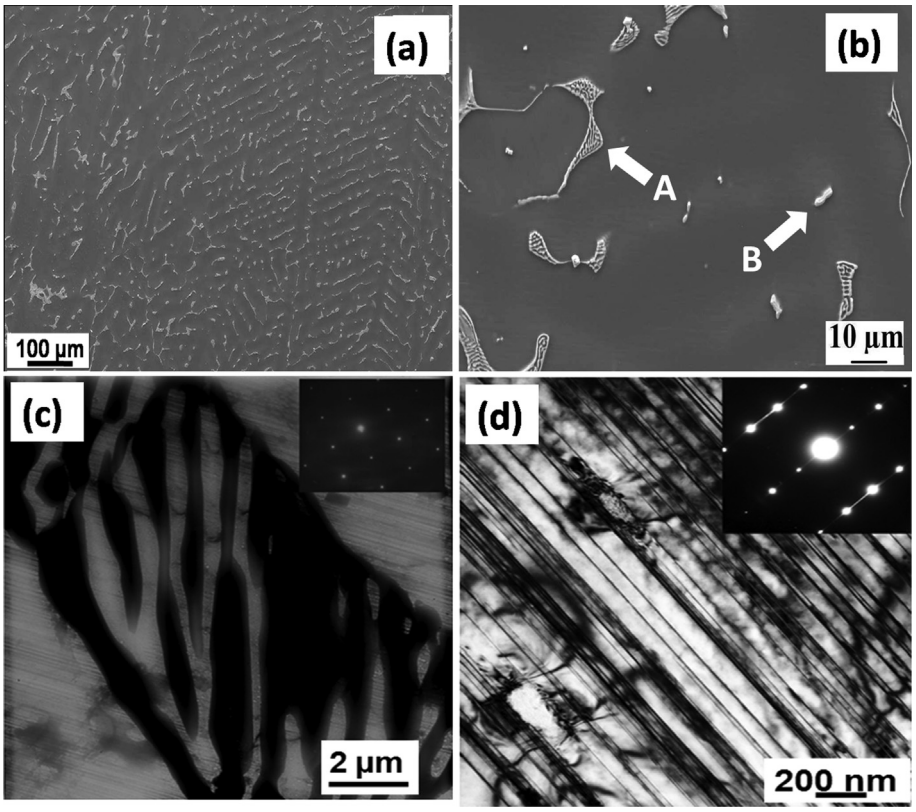

Fig. 1. Microstructure of alloy1 (a) low and (b) high magnified SEM photographs, (c) TEM photograph with SAD pattern of $(Mg,Zn)_3Gd$ phase (electron beam parallel to $<111>_{Mg3Gd}$), (d) TEM micrograph showing the LPSO phase with electron beam parallel to $<1\bar{1}00>_{Mg}$.

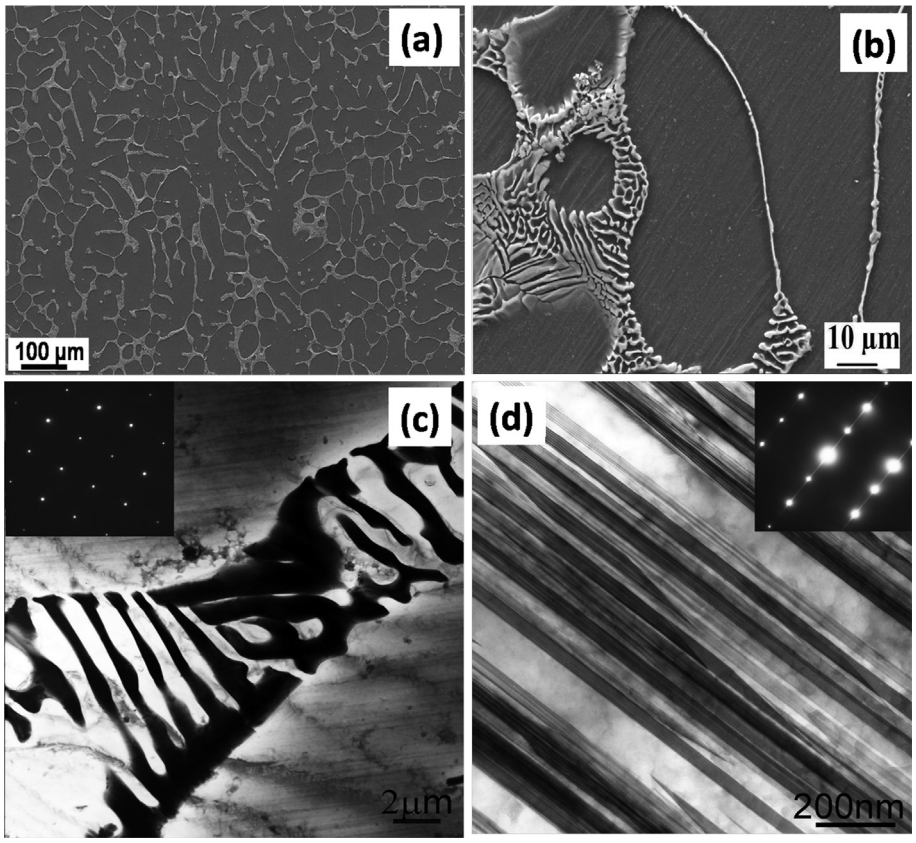

Fig. 2. Microstructure of alloy 2 (a) low and (b) high magnified SEM photographs, (c) TEM photograph with SAD pattern of $(Mg,Zn)_3Gd$ phase (electron beam parallel to <100> Mg_3Gd), (d) TEM micrograph showing the LPSO phase with electron beam parallel to $<1\bar{1}00>_{Mg}$.

and identified as $(Mg, Zn)_3Gd$ type phase as reported in literature [17]. The small particles, which were low in volume fraction (marked as 'B' in Fig. 1(b)), contained equal amount of Gd and Zn content (81.49 at.% Mg-8.62 at.% Gd-8.72 at.% Zn). This phase is similar to $Mg_{12}GdZn$ type phase, which is normally referred as Z or X phase containing LPSO structure. In addition, lamellar LPSO phase in the α-Mg matrix was also observed as evident from Fig. 1(d).

In contrast to alloy 1, the microstructure of alloy 2 consisted of a continuous network of rib bone like phase (Fig. 2(a) & (b)). The EDX spectra taken at different particles showed that the Zn content was slightly higher than the Gd content, and the Zn/Gd ratio was close to 1.5. The TEM analysis (Fig. 2(c)) confirmed the phase to be of Mg_3Gd type with a lattice parameter, $a = 0.732$ nm. This phase was also identified as $(Mg,Zn)_3Gd$ phase similar to that observed in alloy 1, but with slightly different lattice parameters, and appeared as a more continuous network at the interdendritic regions. The TEM investigation also confirmed the presence of fine lamellar LPSO phase (Fig. 2(d)).

3.2. Corrosion behavior

3.2.1. Immersion studies

The main cathodic reaction during corrosion of magnesium alloys is the reduction of hydrogen ions, and hence measuring the volume of hydrogen gas provided the corrosion rate of Mg alloys [18]. The hydrogen evolution curves obtained from eudiometer experiments for the two alloys are shown in Fig. 3. The measurements were conducted until the total amount of hydrogen evolved was just below 400 ml, the maximum capacity of the apparatus. The volume of hydrogen increased with increase in time for both the alloys; however, the rates were different from alloy to alloy as can be seen from Fig. 3.

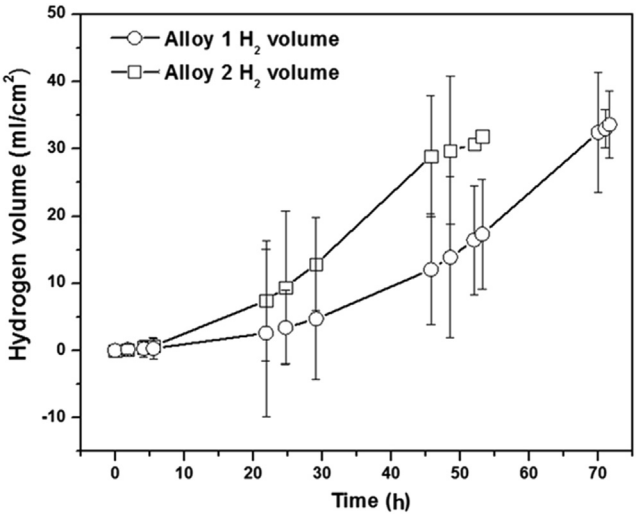

Fig. 3. Hydrogen volume evolution of alloys in 0.5 NaCl solution.

At all the time the slop of the curve for alloy 2 was higher, which indicates that alloy 2 corroded much faster than alloy 1.

The corrosion rates calculated from the hydrogen volumes and the weight loss measurements of the samples used for the eudiometric tests are shown in Fig. 4. Normally, the hydrogen evolution test is valid for the determination of corrosion rates of magnesium alloys. However, the rates calculated from the weight loss measurement showed lower values than that of the corresponding values calculated from the hydrogen evolution measurements. Relatively lower corrosion rates obtained from the weight loss measurements were presumably due to the difficulties faced to remove the corrosion products completely after the test as these samples corroded severely after the long immersion time. However, it is clear that alloy 2 exhibited lower corrosion resistance than that of alloy 1, which, in turn, indicates that the corrosion rate increased as the Zn content in the alloy increased.

3.2.2. Polarization behavior

The polarization curves obtained for the alloys after different immersion times are presented in Fig. 5. The measurements were stopped at the current density of 0.1 mA/cm^2 to avoid much artificial damage on the surface. Normally the idea is to check the ability of the surface to repassivate after the artificial damage during subsequent EIS measurements; however, these two alloys did not passivate again once the active corrosion started. Thus polarization experiments were carried out only in cathodic region. After 0.5 h of immersion (Fig. 5(a)), the alloy 2 showed higher positive potential than that of alloy 1. The cathodic regions of the curves indicated that the cathodic current density of alloy 2 was much higher than that of alloy 1, suggesting that the cathodic hydrogen evolution reaction was much easier in alloy 2 at the beginning of immersion. This was mainly due to the higher volume of second phase in alloy 2, which acted as cathodic sites to initiate corrosion. The polarization behavior of alloys after 24 h immersion (Fig. 5(b)) indicated that the corrosion potential for both alloys became more positive than that observed after 0.5 h immersion, and their cathodic activities were almost similar. Slightly negative potential in comparison with that of 24 h immersion and similar cathodic behavior were observed after 100 h of immersion for both alloys (Fig. 5(c)). The E_{corr} (vs Ag/AgCl) and i_{corr} values obtained from the polarization curves are shown in Table 2. In the present study, the i_{corr} value was calculated from Tafel plot by drawing straight lines from E_{corr} and along the parallel region of the cathodic polarization curve. The current density corresponding to the point of intersection of the lines was taken as i_{corr}. i_{corr} value is direct indicative of the corrosion rate; high i_{corr} value implies high corrosion rate. For both the alloys, as the immersion time increased from 0.5 h to 24 h, the i_{corr} values also increased drastically, and then the increase was not so significant after 100 h immersion. At all the immersion time, the i_{corr} of alloy 2 was higher than that of alloy 1. These polarization results are in line with the corrosion behavior of alloys derived from the hydrogen evolution test.

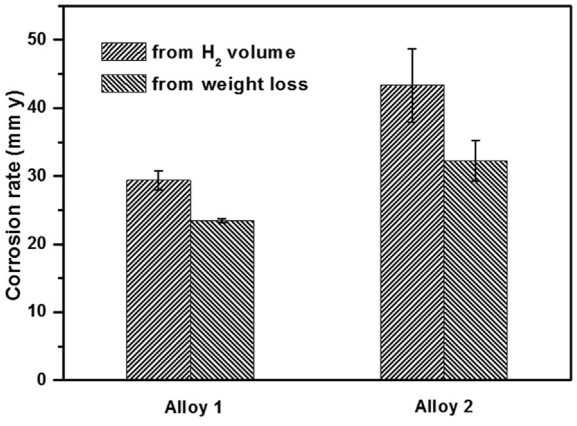

Fig. 4. Corrosion rates of alloys calculated from weight loss and hydrogen measurement.

3.2.3. EIS measurements

EIS measurements of alloys obtained at different immersion times are presented as both Nyquist and Bode plots in Figs. 6 and 7. Most of the magnesium alloys, for instance, AZ91 alloy exhibits three loops in impedance measurements: two capacitive loops and one inductive loop. The high frequency capacitive loop is normally attributed to the charge transfer resistance and double layer capacitance at the metal/solution interface [19]. The medium frequency capacitive loop can be related to the relaxation of mass transport in the solid phase, and this loop disappears after a long immersion time [20]. The inductive loop at the low frequency is attributed to the relaxation processes of adsorbed species on the electrode surface, and can be ascribed to the pit formation [21]. Alloy 1 exhibited only one capacitive loop at all the frequencies after all the immersion times except immediately after the immersion (0 h), where a second semi circle at the lower frequencies was observed (Fig. 6(a)). This low frequency capacitive loop, according to Liu et al. [22], can be related to the corrosion process through the defective surface layer of corrosion product. Normally the charge transfer resistance through the defective surface layer is less than that of the corrosion process occurs at the bare surface of the electrode, which is represented by the high frequency capacitive loop [22].

Alloy 2 showed weak inductive features at the lower frequencies in addition to the single capacitive loop at the higher and medium frequencies (Fig. 7(a)). The inductive loops were relatively strong in the beginning, and as the immersion time increased, this feature became weaker. Weak inductive features were also noticed in alloy 1 (especially after 1 h immersion), however, it was not as apparent as in alloy 2. These inductive loops indicated that more pitting occurred in alloy 2. Normally disappearance or less significance of an induction loop with immersion time is related to the increase in the corrosion resistance (the impedance measurement shows larger capacitive loops) due to a stable film formation [21]. In general, the diameter of the capacitive semi circle is considered as an indicative of the corrosion resistance. The diameter of the capacitive loop initially increased after 1 h immersion,

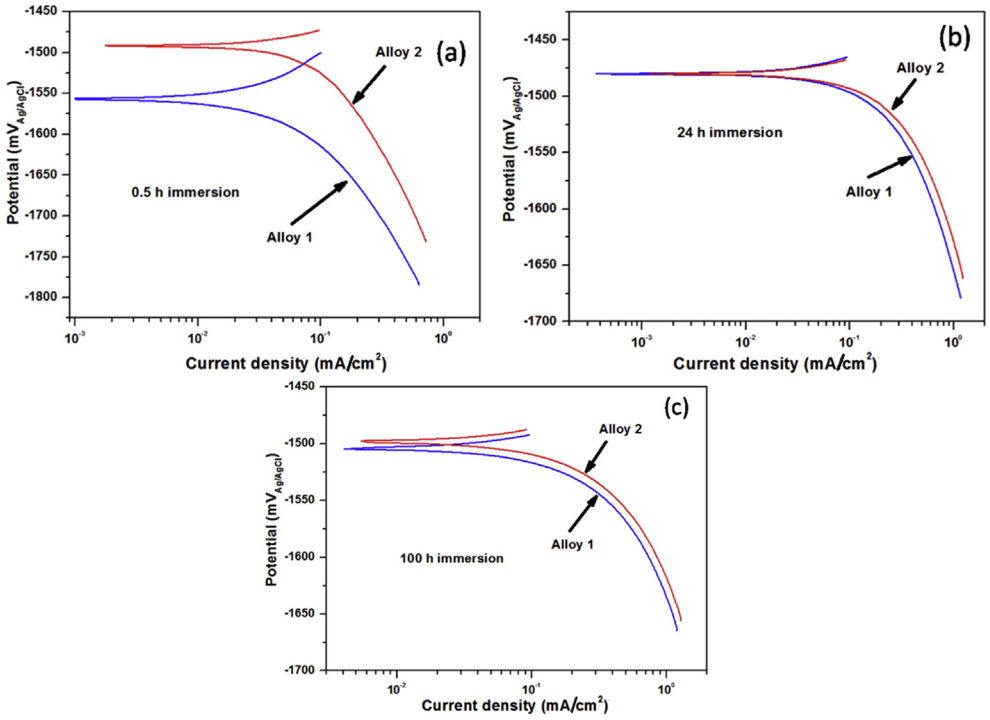

Fig. 5. Polarization behavior of alloys at different immersion times in 0.5 NaCl solution (a) 0.5 h (b) 24 h (c) 100 h.

and then, continuously decreased, as the immersion time increased further for both the alloys. This indicated that a thin weak corrosion layer presented in both alloys in the beginning, but it was not stable and degraded at a faster rate with respect to immersion time. Similar to the present observation, the disappearance of induction loops with increase in immersion times despite increase in corrosion was reported in literature [19,23]. One probable reason may be that the dimensions of the induction loop seem to be connected with the size and severity of the localized corrosion: small pits at the initial stage of corrosion give strong induction loop, and more the corrosion changes to severe localized corrosion, the induction loop becomes less pronounced. In the present study, localized, galvanic corrosion initiated near the second phases at the beginning and it became more severely localized at the grain boundary due to the dissolution of the grain boundary phase itself (will be discussed later). The decrease in corrosion resistance with immersion time was also observed from the impedance values read from the Bode plots at the low frequencies (Figs. 6(b) and 7(b)).

For the further analysis of the impedance spectra, the EIS data were fitted into a simplified equivalent circuit as shown in Fig. 8. The circuit consisted of electrolyte solution resistance (R_s) in series with two parallel combinations of a constant phase element (CPE) and a resistance (R_t-charge transfer resistance and R_f-film resistance). Since weak inductive loops were observed in some of the spectra for alloys 1 and 2, an inductor was also added in series with the resistor in the second time constant. However, as the inductive loops were weak, and also to make the analysis simple, discussion on the results is restricted only to the resistance values of two time constants i.e. R_t and R_f, whose fitted values are presented in Table 3. High R_f value observed in both alloys in the beginning (0 h), indicated the possibility of the existence of a naturally formed thin oxide film on the surfaces, and it became quickly dissolved or transformed in non-protective hydroxide film in the aqueous solution, as the R_f values reduced drastically later (ref. Table 3). The R_t and R_f values for both alloys decreased as the immersion time increased except after 1 h immersion, where an increase in the R_t valves for both alloys was noticed, which represented the impeded dissolution of ions through oxide layer formed in the beginning of corrosion. Immediately after 1 h, the R_f values drastically reduced, and it was stable with further immersion time indicating that no effective passive layer on the surface formed in both alloys during corrosion. The total resistance ($R_t + R_f$) of alloys showed a consistent trend of decreasing. At all immersion times, the resistance values of alloy 2 were much lower than that of alloy 1, however, the difference between the two alloys decreased as the immersion time increased. This showed that both alloys corroded almost at similar rate with alloy 1 still performing slightly better than alloy 2 after prolonged immersion, which matches with the polarization results.

Table 2
E_{corr} (vs Ag/AgCl) and I_{corr} values of alloys obtained from polarization measurement.

Alloy	i_{corr} (mA/cm^2)			E_{corr}(mV)		
	0.5 h	24 h	100 h	0.5 h	24 h	100 h
Alloy 1	0.065	0.128	0.193	−1551	−1480	−1505
Alloy 2	0.110	0.181	0.206	−1495	−1480	−1498

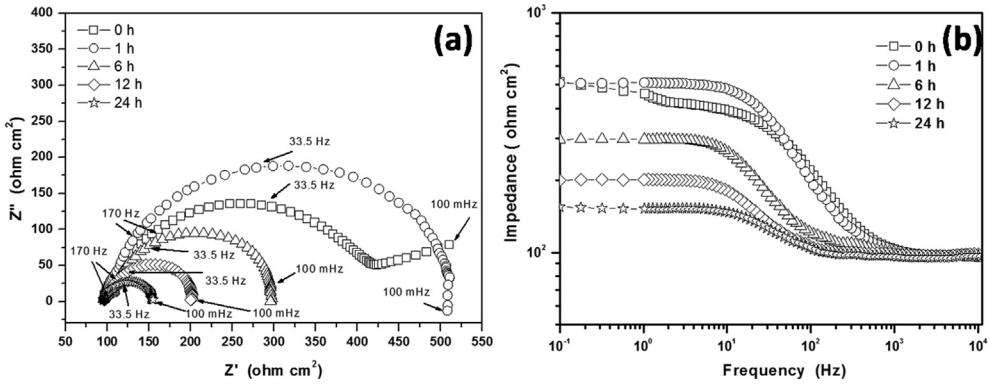

Fig. 6. EIS measurement of alloy 1 at different immersion times (a) Nyquist plot (b) Bode plot.

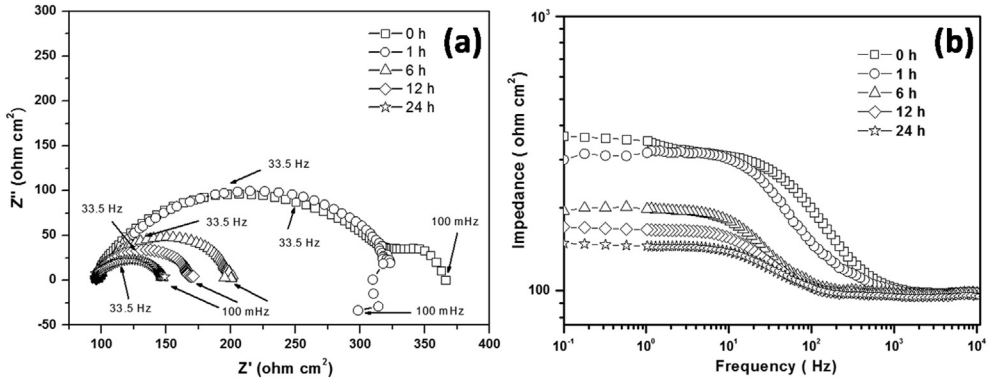

Fig. 7. EIS measurement of alloy 2 at different immersion times (a) Nyquist plot (b) Bode plot.

3.2.4. Corrosion morphology

Fig. 9 shows the macrographs of samples after immersion for different times. Corrosion on both alloys initiated from the edges of the samples and was inhomogeneous (Fig. 9(a) and (d)). A filiform type of corrosion attack was observed in the beginning of the corrosion process. As the immersion time increased the corroded regions on the samples increased (Fig. 9(b) and (e)), however, at all immersion times, the corrosion was severe in alloy 2 compared to alloy 1. After 100 h of immersion, the samples were completely covered by severe deep localized corrosion (Fig. 9(c) and (f)). Again, severe corrosion was observed on alloy 2 with deeper and bigger pits presented all over the surface. A series of SEM micrographs recorded after different immersion times indicated the corrosion morphologies in more details and are presented in Figs. 10 and 11. All the images were taken after the corrosion products were removed, except for the samples that were immersed for 30 min. (Figs. 10(a) and 11(a)) which indicated that the corrosion initiated around the intermetallics in both alloys. Loose round corrosion products appeared on the vicinity of second phases. The second phases and the central regions of Mg matrix were intact suggesting that the corrosion initially occurred in the Mg matrix adjacent to the second phase. As the immersion time increased to 5 h, filiform corrosion dominated in alloy 1 where the corrosion spread like filament (Fig. 10(b)). The onset of filiform corrosion was not known. The corrosion was highly heterogeneous in nature in both the alloys. The severely corroded region of alloy 1 shown in Fig. 10(c) indicates that the filaments spread along the dendrite arms without affecting the intermetallics. The second phases were sitting firmly on the hills of the filaments

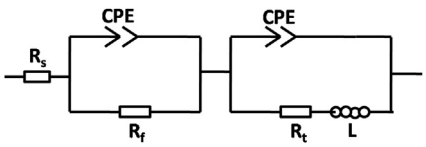

Fig. 8. Equivalent circuit model used to fit the EIS data.

Table 3
Resistance values obtained from the equivalent circuit.

Alloy	Time (h)	R_t (ohm cm^2)	R_f (ohm cm^2)	$R_t + R_f$ (ohm cm^2)
Alloy 1				
	0	337	300	637
	1	399	35	434
	6	190	25	215
	12	104	25	129
	24	46	59	105
Alloy 2				
	0	150	130	280
	1	212	25	237
	6	105	23	128
	12	73	16	89
	24	50	20	70

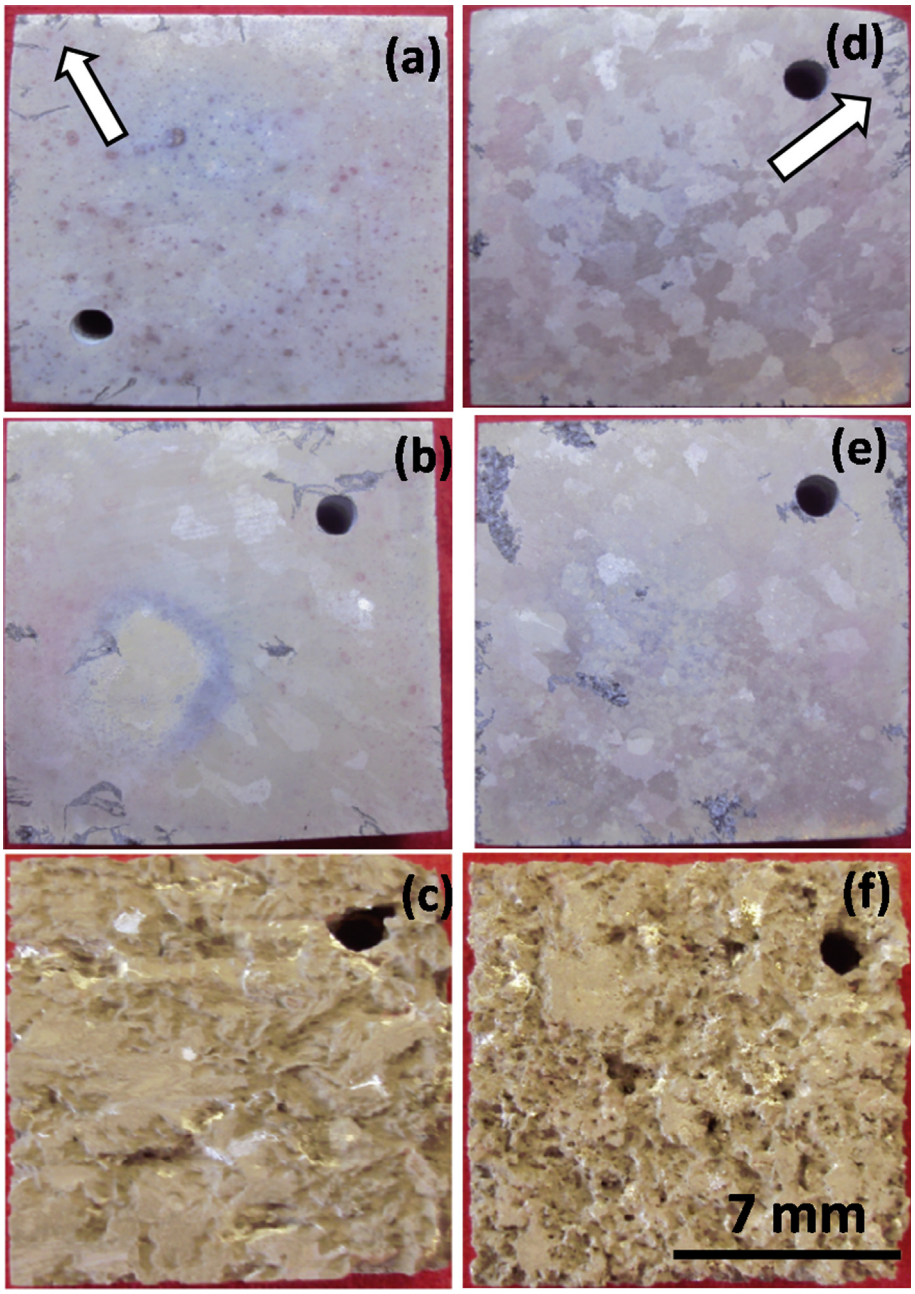

Fig. 9. Macrographs of corroded samples at different immersion times (a) alloy 1 after 2 h (b) alloy 1 after 5 h (c) alloy 1 after 100 h (d) alloy 2 after 2 h (e) alloy 2 after 5 h (f) alloy 2 after 100 h.

suggesting that the second phase was highly stable and acted as cathodic sites during corrosion. Similar filiform corrosion in many magnesium alloys were reported earlier [24,25]. The filaments were also aligned along a particular direction, probably followed a preferred crystallographic direction as reported earlier [26]. Preferred crystallographic pitting (PCP) was also reported in Mg alloys [27]. Micro-galvanic corrosion also occurred simultaneously around the second phase as indicated in Fig. 10(d).

The corrosion morphology of alloy 2 after 5 h of immersion also showed a filament like appearance (Fig. 11(b)), but careful investigation revealed that the features of the filaments were different from that of alloy 1. The filaments were short and wide due to the finer dendrite size and continuous network of second phase particles at the dendrite boundaries. Corrosion in the alloy 2 initiated near the second phase particles (due to micro-galvanic effect) and spread into the grain in both forward and radial direction (Fig. 11(c)). In the later stage, the corrosion morphology looked like filaments. Many small pits were also observed in the non-severely corroded regions along the second phase particles and across the grain, Fig. 11(d). Similar pits appeared also in alloy 1 (micrograph is not shown). After 16 h of immersion, both alloys showed severe corrosion attack (Figs. 10(e) and 11(e)). The corrosion spread through the samples and many wide pits were observed. The most important observation was the complete removal of

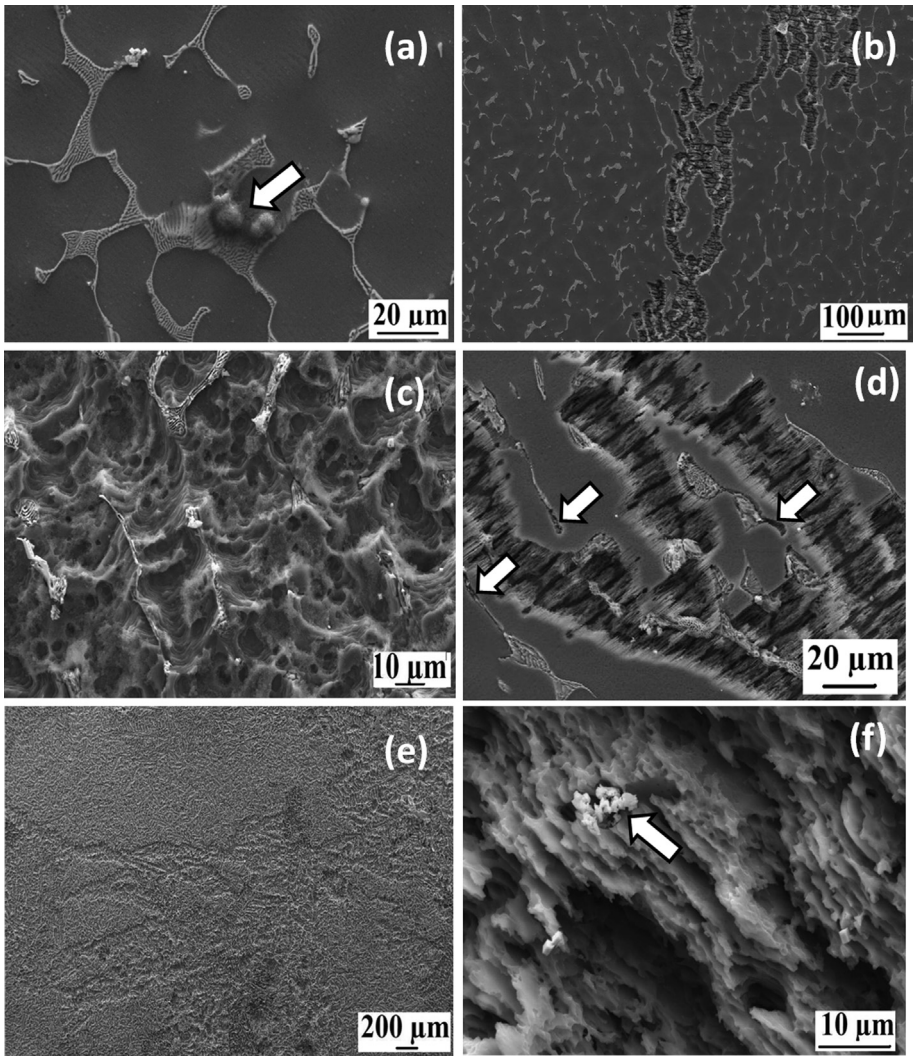

Fig. 10. SEM micrographs showing the corrosion morphologies of alloy 1 after different immersion times (a) 0.5 h (b), (c) & (d) 5 h (e) & (f) 16 h.

second phase particles at the grain boundaries in both alloys. Only magnesium dendrites were clearly seen. Residues of the second phase in some areas could also be seen in both alloys as shown in Fig. 10(f). High magnification microstructure revealed that the corrosion attack in the α-Mg matrix produced striations (Fig. 11(f)). These results suggested that the corrosion mechanisms completely changed during the immersion test.

4. Discussion

Mg−Gd−Zn alloys are relatively new, and their microstructures have been characterized based on the Mg−Zn−Y system which behaves in a similar manner. From the present investigation, it is clear that both alloys contained $(Mg,Zn)_3Gd$ type phase with f.c.c. structure. Literature reports this phase as W−$Mg_3Zn_3Gd_2$ phase similar to the W phase observed in Mg−Zn−Y systems but with slightly different lattice parameters [12]. Recently, Yamasaki et al. [17] reported that the phase was Mg_3Gd type with incorporation of Zn atoms in the magnesium positions of the lattice. In the present study, a slight difference in the lattice parameters of the phases in alloys 1 and 2 was noticed (0.726 nm in alloy 1 and 0.732 nm in alloy 2). This difference might be due to the difference in the compositions of the phases: slightly higher Gd content was observed in alloy 1 whereas Zn/Gd ratio was 1.5 in alloy 2.

Both the simple immersion test (eudiometer test) to the electrochemical tests showed that the alloy 1 performed better than the alloy 2, indicating its better corrosion resistance in 0.5 NaCl solution. However, both alloys cannot be classified as corrosion resistant magnesium alloys, at least in as cast condition. The microstructural features, in particular the second phases, of an alloy are vital factors in deciding its corrosion behavior. In general, most of the second phases in the magnesium alloys are nobler than the magnesium matrix. These noble second phases at the grain boundary form a micro-galvanic couple with the matrix and act as a cathodic sites during the corrosion [28,29]. Extensive research on the corrosion behavior of Mg−Al alloys suggests that the β phase ($Mg_{17}Al_{12}$), when it is present at the grain boundaries in bulk and discontinuous form, is detrimental to the corrosion resistance [30]. Similar micro-galvanic effect was noticed in

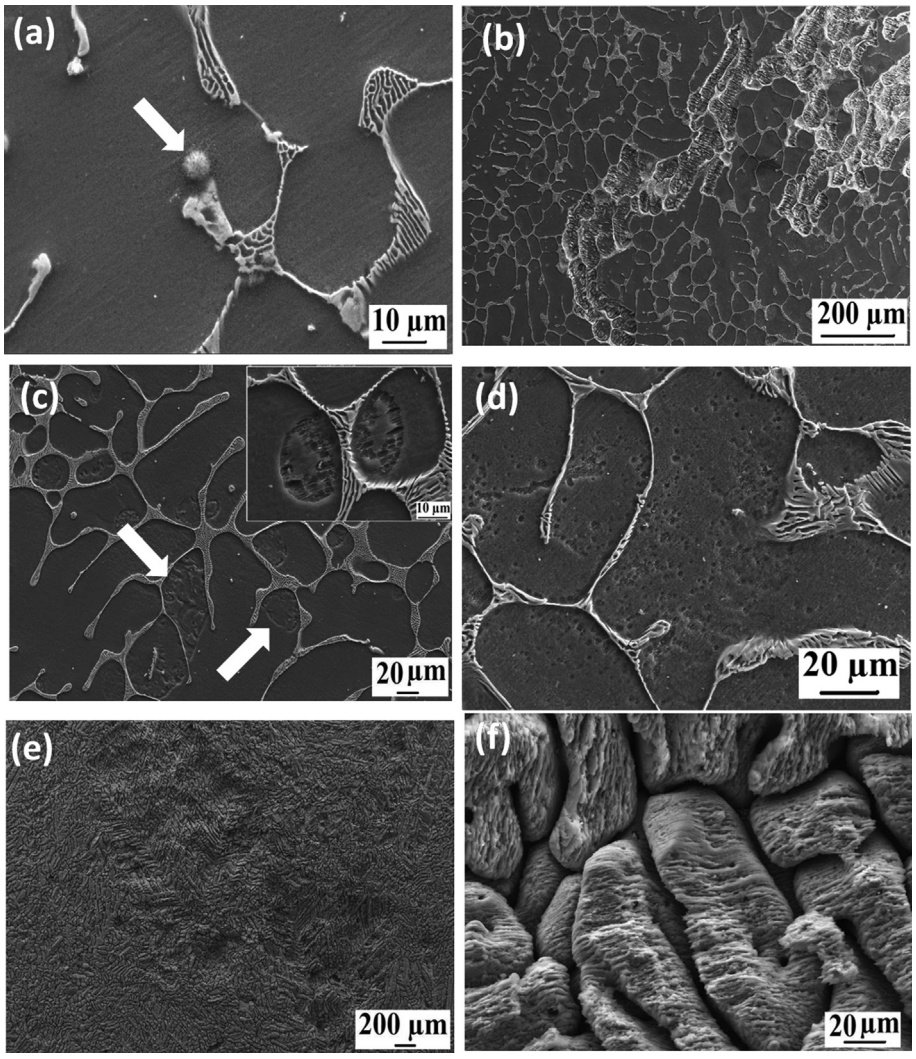

Fig. 11. SEM micrographs showing the corrosion morphology of alloy 2 after different immersion times (a) 0.5 h (b), (c) & (d) 5 h (e) & (f) 16 h.

Mg–Zn alloys where Mg–Zn based intermetallic at the grain boundary induced micro-galvanic corrosion [31]. Moreover, it was observed that the anodic to cathodic area ratio play an important role in the corrosion of magnesium alloys [32]. In addition, it was reported that RE additions to Mg–Al alloys improve its corrosion properties [2,3]. However, corrosion studies on Mg alloys containing RE as major elements, such as Mg–La, Mg–Ce, Mg–Nd and Mg–Y, indicated that corrosion rates increases with increase in RE elements due to the increase in the amount of second phase particles at the grain boundaries [6,33]. Previous studies also reported that micro-galvanic effect due to the second phase particles reduce the corrosion resistance of Mg-RE-Y and Mg-RE-Zn ternary alloys, and when the second phase particles are dissolved in the matrix by solution treatment, the corrosion properties improve drastically, as the rare earth elements in the solid solution stabilizes the surface film [34–36]. In the present study, microstructure investigation suggested that both alloys contained α-Mg, $(Mg,Zn)_3Gd$ and LPSO phases (other minor phases are neglected). However, the major difference was the volume fraction of second phase particles and their morphology. The α-Mg was highly dendritic with fine dendrite arm spacing in alloy 2 whereas it solidified mainly as columnar dendrites in alloy 1. The second phase particles between the dendrite arms were continuous in alloy 2 and more discrete in alloy 1. These microstructural differences resulted in different corrosion morphologies observed.

The initial stage of corrosion of both alloys was mainly due to the micro-galvanic effect of grain boundary second phase. Immediately after the immersion of samples, matrix near the second phase at the grain boundary dissolved preferentially due to micro-galvanic effect, and suggesting that the second phase was nobler than the Mg matrix. Increased volume of second phase in alloy 2 provided more micro-galvanic sites and resulted in faster corrosion rate. In addition to the higher volume fraction of $(Mg,Zn)_3Gd$ phase, there might be a possibility that the difference in the chemical composition of the same intemetallics ($(Mg,Zn)_3Gd$) in the alloys also influenced the severity of the micro-galvanic process. The $(Mg,Zn)_3Gd$ phase in the alloy 2 had more Zn compared to the similar phase in the alloy 1 which consisted of more Gd. A weak protective oxide layer might have formed initially on surfaces of both the alloys

in air, which was evident from the higher initial film resistance observed in the impedance measurement. The higher film resistance value of alloy 1 (300 ohm/cm^2) to that of alloy 2 (130 ohm/cm^2) indicated that the protective film was more effective in alloy 1. Normally, filiform corrosion occurs on coated or anodized surfaces [37]. According to Lunder et al. [24], filiform corrosion may also occur on the uncoated surfaces but in the presence of an oxide film which is resistant to the corrosive environment. Hence, the presence of filiform corrosion morphology observed in the present study suggests that there was an oxide film initially on the surfaces of the samples. However, the corrosion layers seemed to be not stable in both the alloys, and either become a non-protective hydroxide film or collapsed after 1 h of immersion. This is evident from the very low resistance (R_f) values observed in the impedance measurement after 1 h and thereafter (ref. Table 3).

Intergranular corrosion took place in both the alloys at the later stage of corrosion as observed with the microstructure of 16 h immersed samples (Figs. 10(e) and 11(e)). There might be three possibilities for the complete removal of second phases along the boundaries. Micro-galvanic corrosion occurred severely around the second phases and finally, the second phases were undermined during corrosion as observed in other magnesium alloys, especially the Mg–Al alloys [30]. The second possibility was the dissolution of second phase itself in the later stages of corrosion. Careful and repeated microstructural investigation suggested that the probability for the dissolution of this phase was high. The microstructure of alloy 2 immersed for 16 h, shown in Fig. 12, strongly supported the dissolution of eutectic second phase (white regions marked as A) while the eutectic magnesium regions were relatively stable. Dissolution of second phase was possible if the stability of the second phases was altered by NaCl solution, and stronger alkalinization of the surface by the corrosion products after longer times of immersion. The exact onset time for the change in stability of the phase was not known from the present study. Similar observations were made by Neil et al. [25,38] in ZE41 alloy after 18 h of immersion in 0.001 M NaCl. It was claimed that the T-phase (Mg_7Zn_3RE) at the grain boundary was preferentially attacked by the corrosion product removal solution, which was a combination of 200 g CrO_3, 10 g $AgNO_3$, 20 g $Ba(NO_3)$ with reagent water [25,38]. Similarly, it was also possible that chromic acid, which was used for clearing the corrosion product in the present study, might have reacted with the weak second phase during cleaning process and removed it. However, it is worth mentioning that the chromic acid did not attack the second phases in as cast samples that were not immersed in NaCl solution and samples immersed for short times (i.e. 2 and 5 h). Further detailed investigations are in progress to understand this phenomenon. At the moment, it is not clear if the removal of the intermetallics occurred already during the corrosive exposure or during the cleaning step. A third option was also possible considering the fact that there was a protective film on the surface before immersion. Breakdown of this film occurred quite quickly on the matrix regions; however, it might still have existed on the intermetallic phases for a longer period preventing them from dissolution. The intermetallic, although nobler, might be less corrosion resistant in the presence of chloride than the matrix. Considering the protective current flowing from the matrix to the intermetallic and to the protective film on it, there was an onset time for the dissolution of the intermetallics.

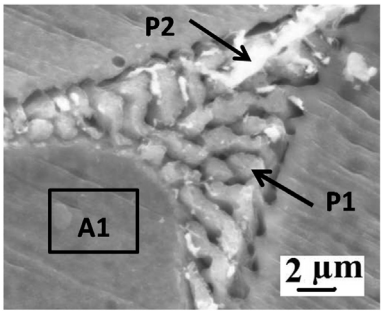

Element	Percentage (At. %)		
	A1	P1	P2
OK	1.56	4.95	17.17
MgK	97.09	92.73	63.88
GdL	0.54	0.89	0.45
ZnK	0.65	0.88	16.51

Fig. 12. SEM micrographs of alloy 2 showing the dissolution of second phase after 16 h immersion.

The role of LPSO phase on the corrosion resistance of the Mg–Zn–RE alloys is not clear from the literature. Zhang et al. [39] reported that the presence of lamellar LPSO phase in the matrix improved the corrosion resistance and uniform corrosion in a Mg–Gd–Zn–Zr alloy. In contrast, Zhang et al. [40] observed that increase in the volume of bulk X phase containing LPSO structure at the grain boundary in Mg–Zn–Y alloys increased the corrosion rate due to the galvanic coupling effect. Izumi et al. [41] studied the effect of cooling rates on the corrosion behavior of Mg–Zn–Y alloys containing LPSO phase, and observed that the presence of the LPSO phases involved in the filiform corrosion process whereas single phase microstructure obtained by higher solidification rate delayed the occurrence of the filiform corrosion. Pérez et al. [42] also observed that the LPSO phase was more preferably attacked by the corrosion when compared to the other intermetallic, $Mg_{12}RE$ in a cast Mg–Zn–Y-MM alloys. The observed filiform corrosion in the present study was probably assisted by the LPSO phase. Severe dissolution of magnesium matrix and striations observed in the microstructure of alloys 1 and 2 (Figs. 10(f) and 11(f)) suggested that LPSO phase facilitated the corrosion in these alloys. Higher corrosion rate observed with alloy 2 can also be related to the higher LPSO phase volume in the matrix expected with the increase in Zn content.

5. Conclusions

Mg–10Gd–xZn (x = 2 and 6%) alloys consisted of $(Mg,Zn)_3Gd$ phase at the grain boundary and lamellar LPSO

phase in matrix. These phases increased as the Zn content increased. The grain boundary phase, $(Mg,Zn)_3Gd$, in Mg−10Gd−6Zn alloy was a continuous network along the highly branched dendrite structure of α-Mg, whereas this phase was relatively discrete in Mg−10Gd−2Zn alloy with microstructure containing mostly columnar α-Mg dendrites. Both hydrogen measurement and electrochemical tests confirmed that increase in the Zn content from 2 to 6% in Mg−10Gd−*x*Zn alloys reduced the corrosion resistance. However, both alloys cannot be classified as corrosion resistant magnesium alloys, at least in as cast condition. Micro-galvanic corrosion due to the presence of second phase at the grain boundary occurred initially in both alloys. However, filiform corrosion dominated at the later stage which was facilitated by the LPSO phase in the matrix. Dissolution of second phase occurred after long immersion times, which was probably due to the change in the stability of the phase altered by NaCl, alkainization of the surface during the long immersion times, and/or by retarded dissolution of the original protective film on the intermetallics. Additionally, it was also possible that the chromic acid might have facilitated the removal of the de-stabilized second phase during the cleaning process.

Acknowledgments

The authors thank Mr. G. Meister for the preparation of alloys, Mrs. Maria Rosario Silva for conducting eudiometer corrosion tests, Mrs. Petra Fischer and Mr. Gert Wiese for SEM investigations. The Alexander von Humboldt (AvH) foundation is acknowledged by the first author for the post doctoral fellowship awarded to him. The first author also acknowledged CSIR-NIIST for deputing him to HZG, Germany.

References

[1] X.W. Guo, J.W. Chang, S.M. He, W.J. Ding, X. Wang, Electrochim. Acta 52 (2007) 2570.
[2] F. Rosalbino, E. Angelini, S.D. Negri, A. Saccone, S. Delfino, Intermetallics 14 (2006) 1487.
[3] F. Rosalbino, E. Angelini, S.D. Negri, A. Saccone, S. Delfino, Intermetallics 13 (2005) 55.
[4] J.D. Hanawalt, C.E. Nelson, J. Peloubet, Trans. AIME 147 (1942) 273.
[5] T. Takenaka, T. Ono, Y. Narazaki, Y. Naka, M. Kawakami, Electrochim. Acta 53 (2007) 117.
[6] N. Birbilis, M.A. Easton, A.D. Sudholz, S.M. Zhu, M.A. Gibson, Corros. Sci. 51 (2009) 683.
[7] J.W. Chang, X.W. Guo, P.H. Fu, L.M. Peng, W.J. Ding, Electrochim. Acta 52 (2007) 3160.
[8] M.C. Zhao, M. Liu, G. Song, A. Atrens, Adv. Eng. Mater. 10 (2008) 104.
[9] Q. Peng, X. Hou, L. Wang, Y. Wu, Z. Cao, L. Wang, Mater. Des. 30 (2009) 292.
[10] L. Yang, Y. Huang, Q. Peng, F. Feyerabend, K.U. Kainer, R. Willumeit, N. Hort, Mater. Sci. Eng. B176 (2011) 1827.
[11] S. Zhang, G.Y. Yuan, C. Lu, W.J. Ding, J. Alloys Compd. 509 (2011) 3515.
[12] Y.J. Wu, X.Q. Zeng, D.L. Lin, L.M. Peng, W.J. Ding, J. Alloys Compd. 477 (2009) 193.
[13] G. Gerardo, R. Guillermo, T. Domonkos, P. Pablo, A. Paloma, S. Andreas, S. Norbert, J. Mater. Sci. 49 (2014) 2714.
[14] S. Zhang, G.Y. Yuan, C. Lu, W.J. Ding, in: W.H. Sillekens, S.R. Agnew, N.R. Neelameggham, S.N. Mathaudhu (Eds.), Magnesium Technology 2011, Wiley, California, 2011, pp. 157−159.
[15] N. Hort, Y. Huang, D. Fechner, M. Störmer, C. Blawert, F. Witte, C. Vogt, H. Drücker, R. Willumeit, K.U. Kainer, F. Feyerabend, Acta. Biomater. 6 (2010) 1714.
[16] www.abc.chemistry.bsu.by/vi/analyser/.
[17] M. Yamasaki, M. Sasaki, M. Nishijima, K. Hiraga, Y. Kawamura, Acta. Mater. 55 (2007) 6798.
[18] M.C. Zhao, M. Liu, G.L. Song, A. Atrens, Corros. Sci. 50 (2008) 3168.
[19] R. Arrabal, A. Pardo, M.C. Merino, M. Mohedano, P. Casajus, K. Paucar, G. Garces, Corros. Sci. 55 (2012) 301.
[20] G. Baril, N. Pebere, Corros. Sci. 43 (2001) 471.
[21] M. Anik, G. Celikten, Corros. Sci. 49 (2007) 1878.
[22] M. Liu, P. Schmutz, P.J. Uggowitzer, G. Song, A. Atrens, Corros. Sci. 52 (2010) 3687.
[23] R. Pinto, M.G.S. Ferreira, M.J. Carmezim, M.F. Montemor, Electrochim. Acta 56 (2011) 1535.
[24] O. Lunder, J.E. Lein, S.M. Hesjevik, T.K. Aune, K. Nisancioglu, Werkst. Korros. 45 (1994) 331.
[25] W.C. Neil, M. Forsyth, P.C. Howlett, C.R. Hutchinson, B.R.W. Hinton, Corros. Sci. 53 (2011) 3299.
[26] P. Schmutz, V. Guillaumin, R.S. Lillard, J.A. Lillard, J. Electrochem. Soc. 150 (2003) B99.
[27] G. Han, J.Y. Lee, Y.C. Kim, J.H. Park, D.I. Kim, H.S. Han, S.J. Yang, H.K. Seok, Corros. Sci. 63 (2012) 316.
[28] H.G. Ben, D. Eliezer, K.S. Shin, Intermetallics 16 (2008) 860.
[29] A. Srinivasan, S. Ningshen, U. Kamachi Mudali, U.T.S. Pillai, B.C. Pai, Intermetallics 15 (2007) 1522.
[30] G. Song, Adv. Eng. Mater. 7 (2005) 563.
[31] Y. Song, E.H. Han, D. Shan, C.D. Yim, B.S. You, Corros. Sci. 60 (2012) 238.
[32] R.K. Singh Raman, Metall. Mater. Trans. 35A (2004) 2525.
[33] A.D. Sudholz, K. Gusieva, X.B. Chen, B.C. Muddle, M.A. Gibson, N. Birbilis, Corros. Sci. 53 (2011) 2277.
[34] R. Pinto, M.G.S. Ferreira, M.J. Carmezim, M.F. Montemor, Electrochim. Acta 55 (2010) 2482.
[35] Y. Song, D. Shan, R. Chen, E.H. Han, Corros. Sci. 52 (2010) 1830.
[36] A.E. Coy, F. Viejo, P. Skeldon, G.E. Thompson, Corros. Sci. 52 (2010) 3896.
[37] R.T. Ruggeri, T.R. Beck, Corrosion 39 (1983) 452.
[38] W.C. Neil, M. Forsyth, P.C. Howlett, C.R. Hutchinson, B.R.W. Hinton, Corros. Sci. 51 (2009) 387.
[39] X. Zhang, Y. Wu, Y. Xue, Z. Wang, L. Yang, Mater. Lett. 86 (2012) 42.
[40] J. Zhang, J. Xu, W. Cheng, C. Chen, J. Kang, J. Mater. Sci. Technol. 28 (2012) 1157.
[41] S. Izumi, M. Yamasaki, Y. Kawamura, Corros. Sci. 51 (2009) 395.
[42] P. Pérez, E. Onofre, S. Cabeza, I. Llorente, J.A. del Valle, M.C. Garćia-Alonso, P. Adeva, Corros. Sci. 69 (2013) 226.